Detecting ionized bubbles in redshifted 21-cm maps

Kanan K. Datta,[1]★ Somnath Bharadwaj[1]★ and T. Roy Choudhury[2]★

[1]*Department of Physics and Meteorology and Centre for Theoretical Studies, IIT, Kharagpur 721302, India*
[2]*Institute of Astronomy, Madingley Road, Cambridge CB3 0HA*

ABSTRACT

The reionization of the Universe, it is believed, occurred by the growth of ionized regions (bubbles) in the neutral intergalactic medium. We study the possibility of detecting these bubbles in radio-interferometric observations of redshifted neutral hydrogen (H I) 21-cm radiation. The signal (<1 mJy) will be buried in noise and foregrounds, the latter being at least a few orders of magnitude stronger than the signal. We develop a visibility based formalism that uses a filter to optimally combine the entire signal from a bubble while minimizing the noise and foreground contributions. This formalism makes definite predictions on the ability to detect an ionized bubble or conclusively rule out its presence in a radio-interferometric observation. We make predictions for the currently functioning Giant Metre-Wave Radio Telescope (GMRT) and a forthcoming instrument, the Mileura Widefield Array (MWA) at a frequency of 150 MHz (corresponding to a redshift of 8.5). For both instruments, we show that a 3σ detection will be possible for a bubble of comoving radius $R_b \geqslant 40$ Mpc (assuming it to be spherical) in 100 h of observation and $R_b \geqslant 22$ Mpc in 1000 h of observation, provided the bubble is at the centre of the field of view. In both these cases, the filter effectively removes the expected foreground contribution so that it is below the signal, and the system noise is the deciding criteria. We find that there is a fundamental limitation on the smallest bubble that can be detected arising from the statistical fluctuations in the H I distribution. Assuming that the H I traces the dark matter, we find that it will not be possible to detect bubbles with $R_b < 8$ Mpc using the GMRT and $R_b < 16$ Mpc using the MWA, however, large be the integration time.

Key words: methods: data analysis – cosmology: theory – diffuse radiation.

1 INTRODUCTION

Quasar absorption spectra (Becker et al. 2001; Fan et al. 2002) and Cosmic Microwave Background Radiation observations (Page et al. 2007; Spergel et al. 2006) together imply that reionization occurred over an extended period spanning the redshift range $6 \leqslant z \leqslant 15$ (for reviews see Choudhury & Ferrara 2006; Fan, Carilli & Keating 2007). It is currently believed that ionized bubbles produced by the first luminous objects grow and finally overlap to completely reionize the Universe (Barkana & Loeb 2001; Furlanetto, Zaldarriaga & Hernquist 2004). In this paper, we consider the possibility of detecting these ionized bubbles in redshifted 21-cm neutral hydrogen (H I) maps.

An ionized bubble embedded in neutral hydrogen will appear as a decrement in the background redshifted 21-cm radiation. This decrement will typically span across several pixels and frequency channels in redshifted 21-cm maps. Detecting this is a big chal-lenge because the H I signal ($\sim$1 mJy or lower) will be buried in foregrounds (Oh 1999; Shaver et al. 1999; DiMatteo et al. 2002; Cooray & Furlanetto 2004; Santos, Cooray & Knox 2005) which are expected to be at least 2–3 orders of magnitude larger. An objective detection criteria which optimally combines the entire signal in the bubble while minimizing contributions from foregrounds, system noise and other such sources is needed to search for ionized bubbles. The noise in different pixels of maps obtained from radio-interferometric observations is correlated (e.g. Thompson, Moran & Swenson 1986), and it is most convenient to deal with visibilities instead. These are the primary quantities that are measured in radio-interferometry. In this paper, we develop a visibility based formalism to detect an ionized bubble or conclusively rule it out in radio-interferometric observations of H I at high redshifts.

The paper is motivated by the fact that the Giant Metre-Wave Radio Telescope (GMRT[1]; Swarup et al. 1991) which is currently functional has a band centred around 150 MHz which corresponds to H I at $z \sim 8.5$. There are several low-frequency radio telescopes

---

★E-mail: kanan@cts.iitkgp.ernet.in (KKD); somnathb@iitkgp.ac.in (SB); chou@ast.cam.ac.uk (TRC)

[1] http://www.gmrt.ncra.tifr.res.in.

which are expected to become functional in the future (e.g. MWA[2], Low Frequency Array[3], 21 CMA[4] and SKA[5]) all of which are being designed to be sensitive to the epoch of reionization H I signal. In this paper, we apply our formalism for detecting ionized bubbles to make predictions for the GMRT and for one of the forthcoming instruments, namely the MWA. For both telescopes, we investigate the feasibility of detecting the bubbles, and in situations where a detection is feasible we predict the required observation time. For both telescopes, we make predictions for observations only at a single frequency (150 MHz), the aim here being to demonstrate the utility of our formalism and not present an exhaustive analysis of the feasibility of detecting ionized bubbles in different scenarios and circumstances. For the GMRT, we have used the telescope parameters from their website, while for the MWA, we use the telescope parameters from Bowman, Morales & Hewitt (2006). It may be noted that MWA is expected to be gradually expanded in phases, and we have used the parameters corresponding to an early stage, the MWA – low-frequency demonstrator.

It is expected that detection of individual bubbles would complement the studies of reionization through the global statistical signal of the redshifted 21-cm radiation which has been studied extensively (e.g. Morales & Hewitt 2004; Zaldarriaga, Furlanetto & Hernquist 2004; Bharadwaj & Ali 2005; Bharadwaj & Pandey 2005; for a recent review see Furlanetto, Oh & Briggs 2006).

The outline of the paper is as follows. In Section 2, we discuss various sources which are expected to contribute in low-frequency radio-interferometric observation, this includes the signal expected from an ionized bubble. In Section 3, we present the formalism for detecting an ionized bubble, and in Section 4, we present the results and discuss its implications. The cosmological parameters used throughout this paper are those determined as the best-fitting values by *Wilkinson Microwave Anisotropy Probe* three-year data release, i.e. $\Omega_m = 0.23$, $\Omega_b h^2 = 0.022$, $n_s = 0.96$, $h = 0.74$, $\sigma_8 = 0.76$ (Spergel et al. 2006).

2 DIFFERENT SOURCES THAT CONTRIBUTE TO LOW-FREQUENCY RADIO OBSERVATIONS

The quantity measured in radio-interferometric observations is the visibility $V(U, \nu)$ which is measured in a number of frequency channels ν across a frequency bandwidth B for every pair of antennas in the array. For an antenna pair, it is convenient to use $U = d/\lambda$ to quantify the antenna separation d projected in the plane perpendicular to the line of sight in units of the observing wavelength λ. We refer to U as a baseline. The visibility is related to the specific intensity pattern on the sky $I_\nu(\theta)$ as

$$V(U, \nu) = \int d^2\theta \, A(\theta) I_\nu(\theta) e^{2\pi i \theta \cdot U}, \qquad (1)$$

where θ is a two-dimensional vector in the plane of the sky with origin at the centre of the field of view and $A(\theta)$ is the beam pattern of the individual antenna. For the GMRT, this can be well approximated by Gaussian $A(\theta) = e^{-\theta^2/\theta_0^2}$ where $\theta_0 \approx 0.6 \, \theta_{FWHM}$ and we use the values $2°.28$ for θ_0 at 153 MHz for the GMRT. Each MWA antenna element consists of 16 crossed dipoles distributed uniformly in a square shaped tile, and this is stationary with respect

to the earth. The MWA beam pattern is quite complicated, and it depends on the pointing angle relative to the zenith (Bowman et al. 2007). Our analysis largely deals with the beam pattern within $1°$ of the pointing angle where it is reasonable to approximate the beam as being circularly symmetric (figs 3 and 5 of Bowman et al. 2007). We approximate the MWA antenna beam pattern as a Gaussian with $\theta_0 = 18°$ at 153 MHz. Note that the MWA primary beam pattern is better modelled as $A(\theta) \propto \cos^2(K\theta)$, but a Gaussian gives a reasonable approximation in the centre of the beam which is the region of interest here. Equation (1) is valid only under the assumption that the field of view is small so that it can be well approximated by a plane, or under the unlikely circumstances that all the antennas are coplanar.

The visibility recorded in 150 MHz radio-interferometric observations is a combination of three separate contributions:

$$V(U, \nu) = S(U, \nu) + N(U, \nu) + F(U, \nu), \qquad (2)$$

where $S(U, \nu)$ is the H I signal that we are interested in, $N(U, \nu)$ is the system noise which is inherent to the measurement and $F(U, \nu)$ is the contribution from other astrophysical sources referred to as the foregrounds. Man-made radio frequency interference (RFI) from cell phones and other communication devices is also expected to contribute to the measured visibilities. Given the lack of a detailed model for the RFI contribution, and anticipating that it may be possible to remove it before the analysis, we do not take it into account here.

2.1 The H I signal from ionized bubbles

According to models of reionization by ultraviolet sources, the early stages of reionization are characterized by ionized H II regions around individual source (QSOs or galaxies). As a first approximation, we consider these regions as ionized spherical bubbles characterized by three parameters, namely, its comoving radius R_b, the redshift of its centre z_c and the position of the centre determined by the two-dimensional vector in the sky-plane θ_c. The bubble is assumed to be embedded in an uniform intergalactic medium (IGM) with a neutral hydrogen fraction x_{HI}. We use r_ν to denote the comoving distance to the redshift where the H I emission, received at a frequency $\nu = 1420 \, MHz/(1 + z)$, originated and defined $r'_\nu = dr_\nu/d\nu$. The planar section through the bubble at a comoving distance r_ν is a disc of comoving radius $R_\nu = R_b\sqrt{1 - (\Delta\nu/\Delta\nu_b)^2}$ where $\Delta\nu = \nu_c - \nu$ is the distance from the bubble centre ν_c in frequency space with $\nu_c = 1420 \, MHz/(1 + z_c)$, and $\Delta\nu_b = R_b/r'_{\nu_c}$ is the bubble size in the frequency space. The bubble, obviously, extends from $\nu_c - \Delta\nu_b$ to $\nu_c + \Delta\nu_b$ in frequency, and in each frequency channel within this frequency range, the image of the ionized bubble is a circular disc of angular radius $\theta_\nu = R_\nu/r_\nu$; the bubble is not seen in H I beyond this frequency range. Under such assumptions, the specific intensity of the redshifted H I emission is

$$I_\nu(\theta) = \bar{I}_\nu x_{HI} \left[1 - \Theta\left(1 - \frac{|\theta - \theta_c|}{\theta_\nu}\right) \right] \Theta\left(1 - \frac{|\nu - \nu_c|}{\Delta\nu_b}\right)$$

$$(3)$$

where $\bar{I}_\nu = 2.5 \times 10^2 \, Jy \, sr^{-1} \left(\frac{\Omega_b h^2}{0.02}\right)\left(\frac{0.7}{h}\right)\left[\frac{H_0}{H(z)}\right]$ is the radiation background from the uniform H I distribution and $\Theta(x)$ is the Heaviside step function.

The soft X-ray emission from the quasar responsible for the ionized region is expected to heat the neutral IGM in a shell around the ionized bubble. The H I emission from this shell is expected to be

[2] http://www.haystack.mit.edu/arrays/MWA.
[3] http://www.lofar.org/.
[4] http://web.phys.cmu.edu/~past/.
[5] http://www.skatelescope.org/.

somewhat higher than $\bar{I}_\nu$ (Wyithe & Loeb 2004). We do not expect this to make a very big contribution, and we do not consider this here.

If we assume that the angular extent of the ionized bubble is small compared to the angular scale of primary beam, that is, $\theta_\nu \ll \theta_0$, we can take $A(\boldsymbol{\theta})$ outside the integral in equation (1) and write the signal as $A(\boldsymbol{\theta}_c) \int d^2\theta I_\nu(\boldsymbol{\theta}) e^{2\pi i \boldsymbol{\theta} \cdot \boldsymbol{U}}$, which essentially involves a Fourier transform of the circular aperture $\Theta(1 - |\boldsymbol{\theta} - \boldsymbol{\theta}_c| r_\nu / R_\nu)$. For example, a bubble of radius as large as 40 Mpc at $z = 8.5$ would have an angular size of only $\theta_\nu \approx 0°.25$ which satisfies the condition $\theta_\nu \ll \theta_0$. In a situation where the bubble is at the centre of the field of view, the visibility is found to be

$$S_{\text{centre}}(\boldsymbol{U}, \nu) = -\pi \bar{I}_\nu x_{\text{HI}} \theta_\nu^2 \left[\frac{2J_1(2\pi U \theta_\nu)}{2\pi U \theta_\nu} \right] \Theta \left(1 - \frac{|\nu - \nu_c|}{\Delta \nu_b} \right), \tag{4}$$

where $J_1(x)$ is the first order Bessel function. Note that $S_{\text{centre}}(\boldsymbol{U}, \nu)$ is real and it is the Fourier transform of a circular aperture. The uniform H I background also contributes $\bar{I}_\nu \pi \theta_0^2 e^{-\pi^2 \theta_0^2 U^2}$ to the visibility, but this has been dropped as it is quite insignificant at the baselines of interest. Note that the approximations used in equation (4) have been tested extensively by comparing the values with the numerical evaluation of the integral in equation (1). We find that the two match to a high level of accuracy for the situations of interest here. In the general situation where the bubble is shifted by $\boldsymbol{\theta}_c$ from the centre of the field of view, the visibility is given by

$$S(\boldsymbol{U}, \nu) = e^{-\theta_c^2/\theta_0^2} e^{2\pi i \boldsymbol{U} \cdot \boldsymbol{\theta}_c} S_{\text{centre}}(\boldsymbol{U}, \nu), \tag{5}$$

that is, there is a phase shift of $e^{2\pi i \boldsymbol{U} \cdot \boldsymbol{\theta}_c}$ and a $e^{-\theta_c^2/\theta_0^2}$ drop in the overall amplitude.

Figs 1 and 2 show the U and $\Delta\nu$ dependence of the visibility signal from an ionized bubble with $R_b = 10$ Mpc located at the centre of the field of view at $\nu_c = 153$ MHz ($z_c = 8.3$), assuming $x_{\text{HI}} = 1$. The signal extends over $\Delta\nu = \pm \Delta\nu_b$ where $\Delta\nu_b = 0.56$ MHz. The extent in frequency $\Delta\nu_b = R_b / r_\nu'$ scales $\propto R_b$ when the bubble size is varied. The Bessel function $J_1(x)$ has the first zero crossing at $x = 3.83$. As a result, the signal $S(\boldsymbol{U}, \nu)$ extends to $U_0 = 0.61 r_\nu [R_b \sqrt{1 - (\Delta\nu/\Delta\nu_b)^2}]^{-1}$ where it has the first zero crossing, and U_0 scales with the bubble size as $U_0 \propto 1/R_b$. The peak value of the signal is $S(0, \nu) = \pi \bar{I}_\nu (R_b / r_\nu)^2 \sqrt{1 - (\Delta\nu/\Delta\nu_b)^2}$ and scales as $S(0, \nu) \propto R_b^2$ if the bubble size is varied. We see that the peak value of the signal is $S(0, \nu_c) = 70 \, \mu$Jy for bubble size $R_b = 10$ Mpc and would increase to 1.75 mJy if $R_b = 50$ Mpc. Detecting these ionized bubbles will be a big challenge because the signal is buried in noise and foregrounds which are both considerably larger
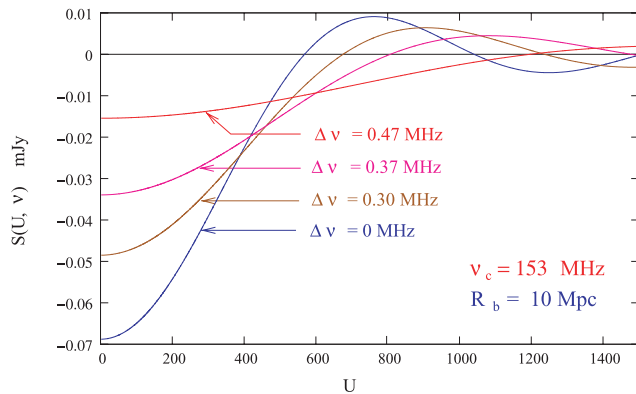
in amplitude. Whether we are able to detect the ionized bubbles or not depends critically on our ability to construct optimal filters which discriminate the signal from other contributions.

2.2 H I fluctuations

In the previous section, we assumed the ionized bubble to be embedded in a perfectly uniform IGM. In reality, however, there would be fluctuations in the H I distribution in the IGM which, in turn, would contribute to the visibilities. This contribution to the H I signal can be treated as a random variable $\hat{S}(\boldsymbol{U}, \nu)$ with zero mean $\langle \hat{S}(\boldsymbol{U}, \nu) \rangle = 0$, whose statistical properties are characterized by the two-visibility correlation $\langle \hat{S}(\boldsymbol{U}_1, \nu_1) \hat{S}(\boldsymbol{U}_2, \nu_2) \rangle$. This is related to $P_{\text{HI}}(\mathbf{k})$ the power spectrum of the 21-cm radiation efficiency in redshift space (Bharadwaj & Ali 2004) through

$$\langle \hat{S}(\boldsymbol{U}_1, \nu) \hat{S}^*(\boldsymbol{U}_2, \nu + \Delta\nu) \rangle = \delta_{\boldsymbol{U}_1, \boldsymbol{U}_2} \frac{\bar{I}_\nu^2 \theta_0^2}{2 r_\nu^2}$$

$$\times \int_0^\infty dk_\parallel \, P_{\text{HI}}(\mathbf{k}) \cos(k_\parallel r_\nu' \Delta\nu), \tag{6}$$

where $\delta_{\boldsymbol{U}_1, \boldsymbol{U}_2}$ is the Kronecker delta, that is, different baselines are uncorrelated. To estimate the contribution from the H I fluctuations (HF), we make the simplifying assumption that the H I traces the dark matter, which gives $P_{\text{HI}}(\mathbf{k}) = \bar{x}_{\text{HI}}^2 (1 + \mu^2)^2 P(k)$ where $P(k)$ is the dark matter power spectrum and μ is the cosine of the angle between $\mathbf{k}$ and the line of sight. This assumption is reasonable because the scales of interest are much larger than the Jeans length $\lambda_J \sim 10$–100 kpc, and we expect the H I to cluster in the same way as the dark matter.

In addition to the above, there could be other contributions to the H I signal too. For example, there would be several other ionized regions in the field of view other than the bubble under consideration. The Poisson noise from these ionized patches will increase the HF and there will also be an overall drop in the contribution because of the reduced neutral fraction. These effects will depend on the reionization model, and the simple assumptions made in this paper would only provide a representative estimate of the actual contribution. Fig. 3 shows the expected contribution from the HF to the individual visibilities for GMRT and MWA. Note that while this can be considerably larger than the signal that we are trying to detect (particularly when the bubble size is small), there is a big difference between the two. The signal from the bubble is correlated across different baselines and frequency channels whereas the
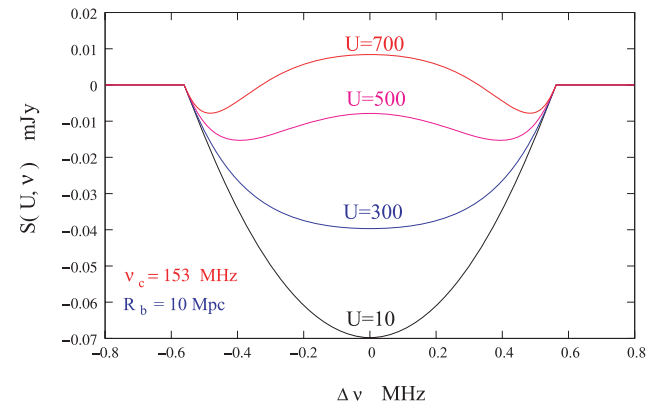

Figure 1. Signal from a spherical ionized bubble of comoving radius 10 Mpc as a function of baseline U for different frequency channels.

Figure 2. Signal from a spherical ionized bubble of comoving radius 10 Mpc as a function of $\Delta\nu = \nu - \nu_c$ for different baselines.
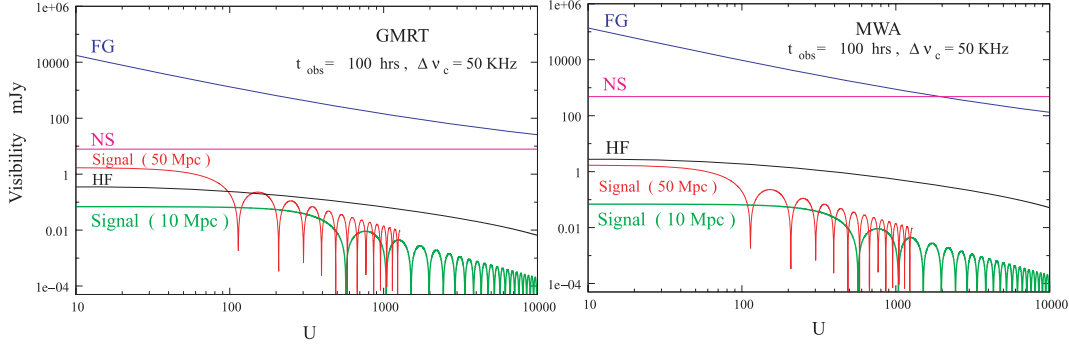
Figure 3. The magnitude of the different contributions to the visibility $V(U, \nu)$ at $\nu = 153$ MHz as a function of U. The signal, FG, NS and HF contributions are shown for the GMRT (left-hand side) and MWA (right-hand side). The expected signal is shown for bubbles with radius $R = 10$ and 50 Mpc. The noise is estimated for a single baseline assuming an observation time $t_{obs} = 100$ h and channel width $\Delta\nu_c = 50$ KHz.

contribution from random HF is uncorrelated at different baselines and it become uncorrelated beyond a certain frequency separation $\Delta\nu$ (Bharadwaj & Ali 2005; Datta, Choudhury & Bharadwaj 2006).

2.3 Noise and foregrounds

The system noise contribution $N(U, \nu)$ in each baseline and frequency channel is expected to be an independent Gaussian random variable with zero mean ($\langle\hat{N}\rangle = 0$) and whose variance is independent of U and ν_c. The predicted rms noise contribution is (Thompson et al. 1986)

$$\sqrt{\langle\hat{N}^2\rangle} = \frac{\sqrt{2}k_B T_{sys}}{A_{eff}\sqrt{\Delta\nu_c\Delta t}}, \tag{7}$$

where T_{sys} is the total system temperature, k_B is the Boltzmann constant, A_{eff} is the effective collecting area of each antenna, $\Delta\nu_c$ is the channel width and Δt is correlator integration time. Equation (7) can be rewritten as

$$\sqrt{\langle\hat{N}^2\rangle} = C^x \left(\frac{\Delta\nu_c}{1\,\text{MHz}}\right)^{-1/2} \left(\frac{\Delta t}{1\text{s}}\right)^{-1/2}, \tag{8}$$

where C^x varies for different interferometric arrays. Using the GMRT parameters, $T_{sys} = 482$ K and $A_{eff}/2k_B = 0.33$ K Jy^{-1} at 153 MHz gives $C^x = 1.03$ Jy for the GMRT where as for MWA $T_{sys} = 470$ K and $A_{eff}/2k_B = 5 \times 10^{-3}$ K Jy^{-1} (Bowman et al. 2006) gives $C^x = 65.52$ Jy. The rms noise is reduced by a factor of $\sqrt{\Delta t/t_{obs}}$ if we average over $t_{obs}/\Delta t$ independent observations where t_{obs} is the total observation time. Fig. 3 shows the expected noise for a single baseline at 153 MHz for $\Delta\nu_c = 50$ KHz and an observation time of 100 h for both the GMRT and MWA. Though T_{sys} is nearly equal for the GMRT and the MWA, the noise in a single baseline is expected to be 60 times larger for MWA than that for the GMRT. This is because the individual antennas have a much larger collecting area at the GMRT as compared to the MWA. The fact that the MWA has many more antennas ($N = 500$) as compared to the GMRT ($N = 30$) compensates for this. Note that nearly half (16) of the GMRT antennas are at very large baselines which are not particularly sensitive to the signal on the angular scales the ionized bubble, and only the other 14 antennas in the 1×1 km central square will contribute towards detecting the signal. For both the GMRT and the MWA, T_{sys} is dominated by the sky contribution T_{sky} with the major contribution coming from our Galaxy. We expect T_{sys} to vary depending on whether the source is in the Galactic plane or away from it. The value which we have used is typical for directions off the Galactic plane. Further, the noise contribution will also be baseline-dependent which is not included in our analysis.

Contributions from astrophysical foregrounds are expected to be several order of magnitude stronger than the H I signal. Extragalactic point sources and synchrotron radiation from our Galaxy are predicted to be the most dominant foreground components. Assuming that the foregrounds are randomly distributed, with possible clustering, we have $\langle\hat{F}(U, \nu)\rangle = 0$ for all the baselines other than the one at zero spacing ($U = 0$), which is not considered in this paper. The statistical properties are characterized by the two-visibility correlation $\langle\hat{F}(U_1, \nu_1)\hat{F}(U_2, \nu_2)\rangle$. We express this [details in Appendix A) in terms of the multi-frequency angular power spectrum (MAPS) $C_l(\nu_1 \nu_2)$ of the brightness temperature fluctuations at the frequencies ν_1 and ν_2 as (Santos et al. 2005; Datta et al. 2006)

$$\langle\hat{F}(U_1, \nu_1)\hat{F}(U_2, \nu_2)\rangle = \delta_{U_1, -U_2}\pi\left(\frac{\theta_1^2\theta_2^2}{\theta_1^2 + \theta_2^2}\right)$$
$$\left(\frac{\partial B}{\partial T}\right)_{\nu_1}\left(\frac{\partial B}{\partial T}\right)_{\nu_2} C_{2\pi U_1}(\nu_1 \nu_2), \tag{9}$$

where $(\partial B/\partial T)_\nu = 2k_B\nu^2/c^2$ is the conversion factor to specific intensity, and we have assumed that the primary beam pattern $A(\theta) = e^{-\theta^2/\theta_0^2}$ is frequency-dependent through $\theta_0 \propto \nu^{-1}$, and use θ_1 and θ_2 to denote the value of θ_0 at ν_1 and ν_2, respectively. Note that the foreground contribution to different baselines is expected to be uncorrelated.

For each component of the foreground, the MAPS is modelled as

$$C_l(\nu_1 \nu_2) = A\left(\frac{\nu_f}{\nu_1}\right)^{\bar{\alpha}}\left(\frac{\nu_f}{\nu_2}\right)^{\bar{\alpha}}\left(\frac{1000}{l}\right)^{\beta} I_l(\nu_1 \nu_2), \tag{10}$$

where $\nu_f = 130$ MHz, and for each foreground component A, β and $\bar{\alpha}$ are the amplitude, the power-law index of the angular power spectrum and the mean spectral index, respectively. The actual spectral index varies with line of sight across the sky and this causes the foreground contribution to decorrelate with increasing frequency separation $\Delta\nu = |\nu_1 - \nu_2|$ which is quantified through the foreground frequency decorrelation function $I_l(\nu_1 \nu_2)$ (Zaldarriaga et al. 2004) which has been modelled as

$$I_l(\nu_1 \nu_2) = \exp\left(-\log_{10}^2\frac{\nu_2/\nu_1}{2\xi^2}\right). \tag{11}$$

We consider the two most dominant foreground components namely extragalactic point sources and the diffuse synchrotron radiation from our own Galaxy. Point sources above a flux level S_{cut} can be identified in high-resolution continuum images and removed. We note that absence of large baselines at the MWA restricts the angular resolution, but it may be possible to use the large frequency

Table 1. Parameters values used for characterizing different foreground contributions

Foregrounds	$A(\mathrm{mK}^2)$	$\bar{\alpha}$	β	ξ
Galactic synchrotron	700	2.80	2.4	4
Point source (clustered part)	$61(\frac{S_{\mathrm{cut}}}{0.1\,\mathrm{mJy}})^{0.5}$	2.07	1.1	2
Point source (Poisson part)	$0.16(\frac{S_{\mathrm{cut}}}{0.1\,\mathrm{mJy}})^{1.25}$	2.07	0	1

bandwidth 32 MHz to identify continuum point sources in the frequency domain. S_{cut} depends on σ the rms noise in the image. We use $S_{\mathrm{cut}} = 5\sigma$ where σ is the rms noise in the image given by (assuming two polarizations)

$$\sigma = \frac{C^x}{\sqrt{2N_b}}\left(\frac{B}{1\,\mathrm{MHz}}\right)^{-1/2}\left(\frac{t_{\mathrm{obs}}}{1\,\mathrm{s}}\right)^{-1/2}, \tag{12}$$

where $N_b = N(N-1)/2$ is the number of independent baselines, N is the number of antennas in the array, B is the total frequency bandwidth and t_{obs} the total observation time. For $t_{\mathrm{obs}} = 100\,\mathrm{h}$ and $B = 6\,\mathrm{MHz}$, we have $S_{\mathrm{cut}} = 0.1\,\mathrm{mJy}$ for the GMRT and using $B = 32\,\mathrm{MHz}$ it gives $S_{\mathrm{cut}} = 0.2\,\mathrm{mJy}$ for the MWA. The value of S_{cut} will be smaller for longer observations, but reducing S_{cut} any further does not make any difference to our results so we hold S_{cut} fixed at these values for the rest of our analysis. The confusion noise from the unresolved point sources is a combination of two parts, the Poisson contribution due to the discrete nature of these sources and the clustering contribution. The amplitudes of these two contributions have different S_{cut} dependence. The parameter values that we have used are listed in Table 1. We have adopted the parameter values from Santos et al. (2005) and incorporated the S_{cut} dependence from DiMatteo et al. (2002).

Fig. 3 shows the expected foreground contributions for the GMRT and MWA. The galactic synchrotron radiation is the most dominant foreground component at large angular scales ($U < 1000$ for GMRT and $U < 2000$ for MWA), while the clustering of the unresolved extragalactic point sources dominates at small angular scales. For all values of U, the foregrounds are at least four orders of magnitude larger than the signal, and also considerably larger than the noise.

The MWA has been designed with the detection of the statistical H I fluctuation signal in mind, and hence it is planned to have a very large field of view. The foreground contribution to a single baseline is expected to be 10 times stronger for the MWA than for the GMRT because of a larger field of view. As we will show later, the increased foreground contribution is not a limitation for detecting H II bubbles. The foregrounds have a continuum spectra, and the contribution at two different frequencies at a separation $\Delta\nu$ is expected to be highly correlated. For $\Delta\nu = 1\,\mathrm{MHz}$, the foreground decorrelation function $I_l(\Delta\nu)$ falls by only 2×10^{-6} for the galactic synchrotron radiation and by 3×10^{-5} for the point sources. In contrast, the signal from an ionized bubble peaks at a frequency corresponding to the bubble centre and falls rapidly with $\Delta\nu$ (Fig. 2). This holds the promise of allowing the signal to be separated from the foregrounds.

3 FORMALISM FOR DETECTING THE IONIZED BUBBLE

We consider a radio-interferometric observation of duration t_{obs}, carried out over the frequency range ν_1 to ν_2. The H I signal from

an ionized bubble, if it is present in the data, will be buried in foregrounds and noise both of which are expected to be much larger. In this section, we present a filtering technique aimed at detecting the signal from an ionized bubble if it is present in our observations. To detect the signal from an ionized bubble of radius R_b with centre at redshift z_c (or frequency ν_c) and at an angle θ_c from the centre of the field of view, we introduce an estimator $\hat{E}[R_b, z_c, \theta_c]$ defined as

$$\hat{E} = \left[\sum_{a,b} S_f^*(U_a, \nu_b)\hat{V}(U_a, \nu_b)\right] \bigg/ \left(\sum_{a,b} 1\right), \tag{13}$$

where $S_f(U, \nu)$ is a filter which has been constructed to detect the particular ionized bubble. Here, U_a and ν_b refer to the different baselines and frequency channels in our observations, and in equation (13) we are to sum over all independent data points (visibilities). Note that the estimator $\hat{E}$ and the filter $S_f(U, \nu)$ both depend on [R_b, z_c, θ_c], the parameters of the bubble we wish to detect, but we do not show this explicitly. The values of these parameters will be clear from the context.

We will be working in the continuum limit where the two sums in equation (13) can be replaced by integrals and we have

$$\hat{E} = \int \mathrm{d}^2U \int \mathrm{d}\nu\, \rho_N(U, \nu)\, S_f^*(U, \nu)\hat{V}(U, \nu) \tag{14}$$

$\mathrm{d}^2U\mathrm{d}\nu\, \rho_N(U, \nu)$ is the fraction of data points, that is, baselines and frequency channels in the interval $\mathrm{d}^2U\,\mathrm{d}\nu$. Note that $\rho_N(U, \nu)$ is usually frequency-dependent, and it is normalized so that $\int \mathrm{d}^2U \int \mathrm{d}\nu\, \rho_N(U, \nu) = 1$. We refer to $\rho_N(U, \nu)$ as the normalized baseline distribution function.

We now calculate $\langle\hat{E}\rangle$, the expectation value of the estimator. Here, the angular brackets denote an average with respect to different realizations of the HF, noise and foregrounds, all of which have been assumed to be random variables with zero mean. This gives $\langle\hat{V}(U, \nu)\rangle = S(U, \nu)$ and

$$\langle\hat{E}\rangle = \int \mathrm{d}^2U \int \mathrm{d}\nu\, \rho_N(U, \nu)\, S_f^*(U, \nu)S(U, \nu). \tag{15}$$

We next calculate the variance of the estimator which is the sum of the contributions from the noise (NS), the foregrounds (FG) and the HF

$$\langle(\Delta\hat{E})^2\rangle \equiv \langle(\hat{E} - \langle\hat{E}\rangle)^2\rangle$$
$$= \langle(\Delta\hat{E})^2\rangle_{\mathrm{NS}} + \langle(\Delta\hat{E})^2\rangle_{\mathrm{FG}} + \langle(\Delta\hat{E})^2\rangle_{\mathrm{HF}}. \tag{16}$$

To calculate the noise contribution, we go back to equation (13) and use the fact that the noise in different baselines and frequency channels are uncorrelated. We have

$$\langle(\Delta\hat{E})^2\rangle_{\mathrm{NS}} = \langle\hat{N}^2\rangle\left[\sum_{a,b}|S_f(U_a, \nu_b)|^2\right]\bigg/\left(\sum_{a,b} 1\right)^2 \tag{17}$$

which in the continuum limit is

$$\langle(\Delta\hat{E})^2\rangle_{\mathrm{NS}} = \left[\langle\hat{N}^2\rangle\bigg/\sum_{a,b} 1\right]$$
$$\times \int \mathrm{d}^2U \int \mathrm{d}\nu\, \rho_N(U, \nu)\,|S_f(U, \nu)|^2. \tag{18}$$

The term $\sqrt{[\langle\hat{N}^2\rangle/\sum_{a,b} 1]}$ is the same as σ, the rms noise in the image equation (12). We then have

$$\langle(\Delta\hat{E})^2\rangle_{\mathrm{NS}} = \sigma^2 \int \mathrm{d}^2U \int \mathrm{d}\nu\, \rho_N(U, \nu)\,|S_f(U, \nu)|^2. \tag{19}$$

For the foreground contribution, we have

$$
\langle (\Delta \hat{E})^2 \rangle_{FG} = \int d^2 U_1 \int d^2 U_2 \int d\nu_1 \int d\nu_2
$$
$$
\times \, \rho_N(\boldsymbol{U}_1, \nu_1) \rho_N(\boldsymbol{U}_2, \nu_2) S_f^*(\boldsymbol{U}_1, \nu_1) S_f^*(\boldsymbol{U}_2, \nu_2)
$$
$$
\times \, \langle \hat{F}(\boldsymbol{U}_1, \nu_1) \hat{F}(\boldsymbol{U}_2, \nu_2) \rangle. \tag{20}
$$

In the continuum limit, we have (details given in Appendix A)

$$
\langle \hat{F}(\boldsymbol{U}_1, \nu_1) \hat{F}(\boldsymbol{U}_2, \nu_2) \rangle = \delta_D^{(2)}(\boldsymbol{U}_1 + \boldsymbol{U}_2) \left(\frac{\partial B}{\partial T} \right)_{\nu_1} \left(\frac{\partial B}{\partial T} \right)_{\nu_2} \tag{21}
$$
$$
\times \, C_{2\pi U_1}(\nu_1, \nu_2)
$$

which gives the variance of the foreground contribution to be

$$
\langle (\Delta \hat{E})^2 \rangle_{FG} = \int d^2 U \int d\nu_1 \int d\nu_2 \left(\frac{\partial B}{\partial T} \right)_{\nu_1} \left(\frac{\partial B}{\partial T} \right)_{\nu_2}
$$
$$
\times \, \rho_N(\boldsymbol{U}, \nu_1) \rho_N(\boldsymbol{U}, \nu_2) S_f^*(\boldsymbol{U}, \nu_1) S_f(\boldsymbol{U}, \nu_2)
$$
$$
\times \, C_{2\pi U}(\nu_1, \nu_2). \tag{22}
$$

We use equation (22) to calculate $\langle (\Delta \hat{E})^2 \rangle_{HF}$ too, with the difference that we use the power spectrum $C_{2\pi U}(\nu, \nu + \Delta \nu)$ for the H I fluctuation from Datta et al. (2006) instead of the foreground contribution.

In an observation it will be possible to detect the presence of an ionized bubble having parameters $[R_b, z_c, \theta_c]$ at, say 3σ confidence level, if $\langle \hat{E} \rangle \geqslant 3\sqrt{\langle (\Delta \hat{E})^2 \rangle}$. In such a situation, an observed value E_o can be interpreted as a detection with 99.7 per cent (i.e. 3σ) confidence if $E_o > 3\sqrt{\langle (\Delta \hat{E})^2 \rangle}$. The presence of the ionized bubble can be ruled out at the same level of confidence if $\langle \hat{E} \rangle - E_o > 3\sqrt{\langle (\Delta \hat{E})^2 \rangle}$.

3.1 Baseline distribution

In this section, we discuss the normalized baseline distribution function $\rho_N(\boldsymbol{U}, \nu)$ which has been introduced earlier. Fig. 4 shows the baseline coverage for 14 h of observation towards a region at declination $\delta = 45°$ with the GMRT at 153 MHz. In this figure, u and v refer to the Cartesian components of the baselines $\boldsymbol{U}$. Note that the baseline distribution is not exactly circularly symmetric. This asymmetry depends on the source declination which would be different for every observation. We make the simplifying assumption
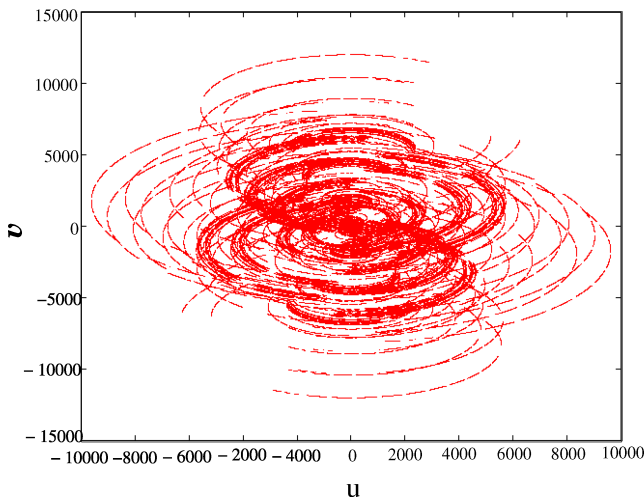

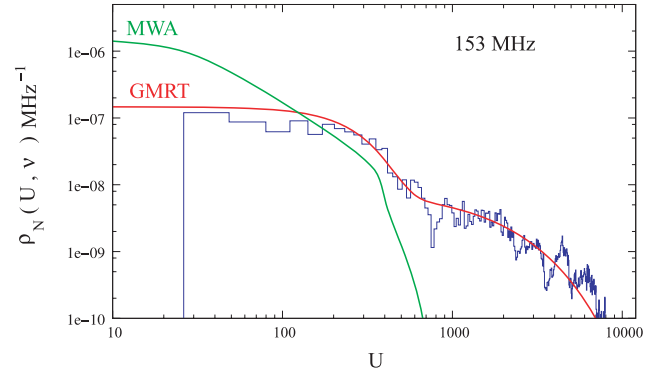**Figure 4.** This shows the baseline coverage for 14 h of GMRT 153 MHz observation at 45° declination.

Figure 5. This shows the normalized baseline distribution $\rho_N(U, \nu)$ for the GMRT and the MWA at 153 MHz. The wiggly curve shows the actual values for the GMRT observation shown in Fig. 4 and the smooth curve is the analytic fit.

that the baseline distribution is circularly symmetric whereby $\rho_N(\boldsymbol{U}, \nu)$ is a function of U. This considerably simplifies our analysis and gives reasonable estimates of what we would expect over a range of declinations. Fig. 5 shows $\rho_N(\boldsymbol{U}, \nu)$ for the GMRT determined from the baseline coverage shown in Fig. 4. We find that this is well described by the sum of a Gaussian and an exponential distribution. The GMRT has a hybrid antenna distribution (Chengalur, Gupta & Dwarkanath 2003) with 14 antennas being randomly distributed in a central square approximately 1×1 km and 16 antennas being distributed along a Y-axis each of whose arms is 14 km long. The Gaussian gives a good fit at small baselines in the central square and the exponential fits the large baselines. Determining the best-fitting parameters using a least square gives

$$
\rho_N(\boldsymbol{U}, \nu) = \frac{1}{B} \left(\frac{\lambda}{1\,\mathrm{km}} \right)^2 \left[0.21 \exp \left(-\frac{U\lambda}{2a^2} \right) \right.
$$
$$
\left. + \, 9.70 \times 10^{-3} \exp \left(-\frac{U\lambda - b}{d} \right) \right], \tag{23}
$$

where $a = 0.382$ km, $b = 0.986$ km, $d = 3.07$ km and B is the frequency bandwidth which has a maximum value of 6 MHz.

Following Bowman et al. (2006), we assume that the MWA antennas are distributed within a radius of 0.750 km with the density of antennas decreasing with radius r as $\rho_{ant}(r) \propto r^{-2}$ and with a maximum density of one antenna per $18\,\mathrm{m}^2$. The normalized baseline distribution is estimated in terms of $\rho_{ant}(r)$ and we have

$$
\rho_N(\boldsymbol{U}, \nu) = \frac{1}{4.4 \times 10^2} \frac{1}{B} \left(\frac{\lambda}{1\,\mathrm{km}} \right)^2 \int_{r=0}^{\infty} d^2 r \, \rho_{ant}(r)
$$
$$
\times \int_{\phi=0}^{2\pi} \rho_{ant}(|\boldsymbol{r} - \lambda \boldsymbol{U}|) d\phi, \tag{24}
$$

where the bandwidth B is 32 MHz, $|\boldsymbol{r} - \lambda \boldsymbol{U}| = (r^2 + U^2 \lambda^2 - 2r \lambda U \cos \phi)^{1/2}$. Note that $\rho_N(\boldsymbol{U}, \nu)$ depends on the observed frequency. Fig. 5 shows the normalized baseline distribution function $\rho_N(\boldsymbol{U}, \nu)$ for both the GMRT and the MWA. We see that maximum baseline for the GMRT is $U_{max} \sim 10\,000$ whereas $U_{max} \sim 750$ for the MWA. However, the smaller baselines will be sampled more densely in the MWA as compared to the GMRT.

3.2 Filter

It is a major challenge to detect the signal which is expected to be buried in noise and foregrounds both of which are much stronger
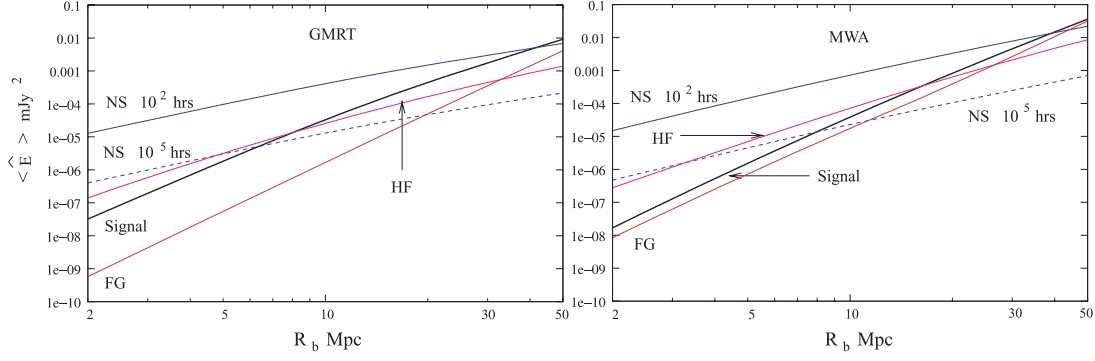
Figure 6. The signal quantified through the expectation value of the estimator $\langle \hat{E} \rangle$ for Filter I. The other components (NS, FG, HF) are quantified through their contribution to the 3σ fluctuation $3 \times \sqrt{\langle (\Delta \hat{E})^2 \rangle}$.

(Fig. 3). It would be relatively simple to detect the signal in a situation where there is only noise and no foregrounds. The signal-to-noise ratio (S/N) is maximum if we use the signal that we wish to detect as the filter (i.e. $S_f(\boldsymbol{U}, \nu) = S(\boldsymbol{U}, \nu)$) and the S/N has a value

$$\frac{\langle (\hat{E}) \rangle}{\sqrt{\langle (\Delta \hat{E})^2 \rangle_{\text{NS}}}} = \frac{1}{\sigma} \left[\int d^2 U \int d\nu \, \rho_N(\boldsymbol{U}, \nu) \mid S(\boldsymbol{U}, \nu) \mid^2 \right]^{0.5}$$
$$\propto \sqrt{t_{\text{obs}}}. \tag{25}$$

The observing time necessary for a 3σ detection (i.e. S/N =3) would be the least for this filter. The difficulty with using this filter is that the foreground contribution to $\sqrt{\langle (\Delta \hat{E})^2 \rangle}$ is orders of magnitude more than $\langle (\hat{E}) \rangle$. The foregrounds, unlike the H I signal, are all expected to have a smooth frequency dependence and one requires filters which incorporate this fact so as to reduce the foreground contribution. We consider two different filters which reduce the foreground contribution, but it occurs at the expense of reducing the S/N and t_{obs} would be more than that predicted by equation (25).

The first filter (Filter I) subtracts out any frequency independent component from the frequency range $\nu_c - B'/2$ to $\nu_c + B'/2$ with $B' \leqslant B$, that is,

$$S_f(\boldsymbol{U}, \nu) = \left(\frac{\lambda_c}{\lambda} \right)^2 [S(\boldsymbol{U}, \nu)$$
$$- \frac{\Theta(1 - 2 \mid \nu - \nu_c \mid /B')}{B'} \int_{\nu_c - B'/2}^{\nu_c + B'/2} S(\boldsymbol{U}, \nu') d\nu' \Big]. \tag{26}$$

This filter has the advantage that it does not require any prior knowledge about the foregrounds except that they have a continuous spectrum. It has the drawback that there will be contributions from the residual foregrounds as all the foregrounds are expected to have a power-law spectral dependence and not a constant. A larger value of B' causes the S/N to increases, and in the limit $B' \to \infty$ the S/N approaches the value given in equation (25). Unfortunately, the residues in the foregrounds also increase with B'. We use $B' = 4 \Delta\nu_b$ provided it is less than B, and $B' = B$ otherwise.

The frequency dependence of the total foreground contribution can be expanded in Taylor series. Retaining terms only up to the first order, we have

$$C_l(\nu_1, \nu_2) = C_l(\nu_c, \nu_c) [1 - (\Delta\nu_1 + \Delta\nu_2) \alpha_{\text{eff}}/\nu_c], \tag{27}$$

where $\Delta\nu = \nu - \nu_c$ and $\alpha_{\text{eff}} = \frac{\sum_i \alpha^i A^i (1000/l)^{\beta_i}}{\sum_i A^i (1000/l)^{\beta_i}}$ is the effective spectral index; here, i refers to the different foreground components. Note

that α_{eff} is l-dependent. The second filter that we consider (Filter II) allows for a linear frequency dependence of the foregrounds and we have

$$S_f(\boldsymbol{U}, \nu) = (1 + \alpha_{\text{eff}} \Delta\nu/\nu_c) \left(\frac{\lambda_c}{\lambda} \right)^2 [S(\boldsymbol{U}, \nu)$$
$$- \frac{\Theta(1 - 2 \mid \nu - \nu_c \mid /B')}{B'} \int_{\nu_c - B'/2}^{\nu_c + B'/2} S(\boldsymbol{U}, \nu') d\nu' \Big]. \tag{28}$$

Note that for both the filters, we include an extra factor $(\lambda_c/\lambda)^2$. This is introduced with the purpose of cancelling out the λ^2 dependence of the normalized baseline distribution function $\rho_N(\boldsymbol{U}, \nu)$ and this substantially reduces the foreground contribution.

4 RESULTS AND DISCUSSIONS

We first consider the most optimistic situation where the bubble is at the centre of the field of view and the filter centre is exactly matched with the bubble centre. The size distribution of H II regions is quite uncertain, and would depend on the reionization history and on the distribution of ionizing sources. However, there are some indications in the literature on what could be the typical size of H II regions. For example, Wyithe, Loeb & Barnes (2005) deduce from proximity zone effects that $R_b \approx 35$ Mpc at $z \approx 6$, which should be considered as a lower limit. On the other hand, Furlanetto, McQuinn & Hernquist (2006) [Fig. 1(a)] infer that the characteristic bubble size $R_b > 10$ Mpc at $z = 8$ if the ionized fraction $x_i > 0.75$ ($R_b \sim 50$ Mpc if $x_i \sim 0.9$). Theoretical models which match a variety of observations (Choudhury & Ferrara 2007) imply that x_i could be as high as 90 per cent at $z \sim 8$, which would mean bubble sizes of ~ 40–50 Mpc. To allow for the large variety of possibilities, we have presented results for a wide range of R_b values from 2 to 50 Mpc. We restrict our analysis to a situation where the IGM outside the bubble is completely neutral ($x_{\text{H I}} = 1$). The signal would fall proportional to $x_{\text{H I}}$ if the IGM outside the bubble were partially ionized ($x_{\text{H I}} < 1$). The expected signal $\langle \hat{E} \rangle$ and 3σ fluctuation $3 \times \sqrt{\langle (\Delta \hat{E})^2 \rangle}$ from each of the different components discussed in Sections 2 and 3 as a function of bubble size R_b are shown in Figs 6 and 7. Both the figures show exactly the same quantities, the only difference being that they refer to Filter I and II, respectively. A detection is possible only in situations where $\langle \hat{E} \rangle > 3 \times \sqrt{\langle (\Delta \hat{E})^2 \rangle}$, the right-hand side now refers to the total contribution to the estimator variance from all the components.
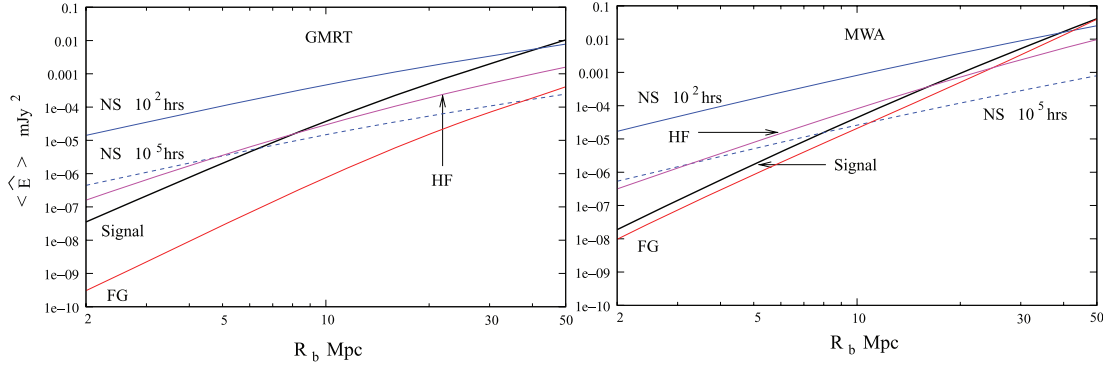
Figure 7. Same as Fig. 6 except that Filter II is used instead of Filter I.

Figure 8. The observing time t_{obs} that would be required for a 3σ detection of a bubble of radius R_b provided it is at the centre of the field of view. The vertical lines show the lower limit (due to HF) where a detection will be possible ($R_b = 8$ Mpc for GMRT and $R_b = 16$ Mpc for MWA).

The signal is expected to scale as R_b^3 and the noise as $R_b^{3/2}$ in a situation where the baseline distribution is uniform, that is, $\rho_N(U, \nu)$ is independent of U. This holds at $U < 300$ for the GMRT (Fig. 5), and the expected scaling is seen for $R_b \geqslant 20$ Mpc. For smaller bubbles, the signal extends to larger baselines where $\rho_N(U, \nu)$ falls sharply, and the signal and the noise both have a steeper R_b dependence. The MWA baseline distribution is flat for only a small U range (Fig. 5) beyond which it drops. In this case, the signal and noise are found to scale as R_b^4 and R_b^2, respectively. Note that the maximum baseline at MWA is $U = 750$, and hence a considerable amount of the signal is lost for $R_b < 10$ Mpc.

At both the GMRT and the MWA, for 100 h of observation, the noise is larger than the signal for bubble size $R_b \leqslant 40$ Mpc. At the other extreme, for an integration time of 10^5 h the noise is below the signal for $R_b > 6$ Mpc for the GMRT and $R_b > 8$ Mpc for the MWA. The foreground contribution turns out to be smaller than the signal for the entire range of bubble sizes that we have considered, thus justifying our choice of filters. Note that Filter II is more efficient in foreground subtraction, but it requires prior knowledge about the frequency dependence. For both the filters the foreground removal is more effective at the GMRT than the MWA because of the frequency dependence of $\rho_N(U, \nu)$. The assumption that this is proportional to λ^2 is valid only when $\rho(U, \nu)$ is independent of U, which, as we have discussed, is true for a large U range at the GMRT. The λ dependence is much more complicated at the MWA, but we have not considered such details here as the foreground contribution is anyway smaller than the signal. It should also be noted that the foreground contribution increases at small baselines equation (10), and is very sensitive to the smallest value of U which we set at $U = 20$ for our calculations. Here, it must be noted that our results are valid only under the assumption that the foregrounds have a smooth frequency dependence. A slight deviation from this and the signal will be swamped by the foregrounds. Also note that this filtering method is effective only for the detection of the bubbles and not for the statistical HF signal.

The contribution from the HF imposes a lower limit on the size of the bubble which can be detected. However, long be the observing time, it will not be possible to detect bubbles of size $R_b < 8$ Mpc using the GMRT and size $R_b < 16$ Mpc using the MWA. The H I fluctuation contribution increases at small baselines. The problem is particularly severe at MWA because of the dense sampling of the small baselines and the very large field of view. We note that the MWA is being designed with the detection of the statistical H I fluctuation signal in mind, and hence it is not surprising that this contribution is quite large. For both telescopes it may be possible to reduce this component by cutting-off the filter at small baselines.
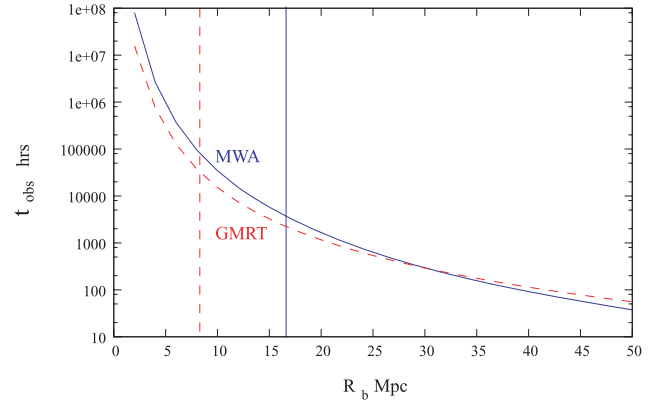
We have not explored this possibility in this work because the enormous observing times required to detect such small bubbles makes it unfeasible with the GMRT or the MWA.

Fig. 8 shows the observation time that would be required to detect bubbles of different sizes using Filter I for the GMRT and the MWA. Note that the observing time shown here refers to a 3σ detection which is possibly adequate for targeted searches centred on observed quasar position. A more stringent detection criteria at the 5σ level would be appropriate for a blind search. The observing time would go up by a factor of 3 for a 5σ detection. The observing time is similar for Filter II, and hence we do not show this separately. In calculating the observing time, we have only taken into account the noise contribution as the other contributions do not change with time. The value of R_b below which a detection is not possible due to the HF is shown by vertical lines for both telescopes. We see that with 100 h of observation both the telescopes will be able to detect bubbles with $R_b > 40$ Mpc while bubbles with $R_b > 22$ Mpc can be detected with 1000 h of observation.

The possibility of detecting a bubble is less when the bubble centre does not coincide with the centre of the field of view. In fact, the S/N falls as $e^{-\theta_c^2/\theta_0^2}$ if the bubble centre is shifted away by θ_c from the centre of the field of view and the filter is also shifted so that its centre coincides with that of the bubble. There will be a corresponding increase $t_{obs} \propto e^{2\theta_c^2/\theta_0^2}$ in the observing time required to detect the bubble. It will be possible to detect bubbles only if they are located near the centre of the field of view ($\theta_c \ll \theta_0$), and the
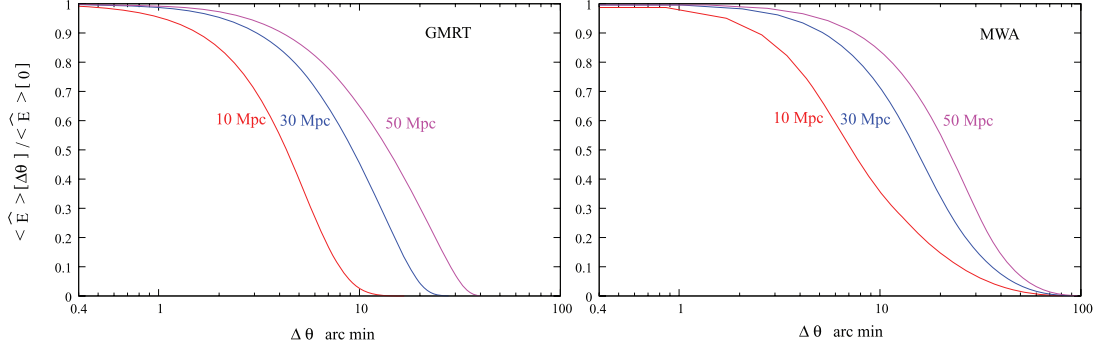
Figure 9. The Overlap between the signal and the filter when there is a mismatch $\Delta\theta$ between the centres of the bubble and the filter for GMRT (left-hand side) and MWA (right-hand side). The results are shown for different bubble sizes.
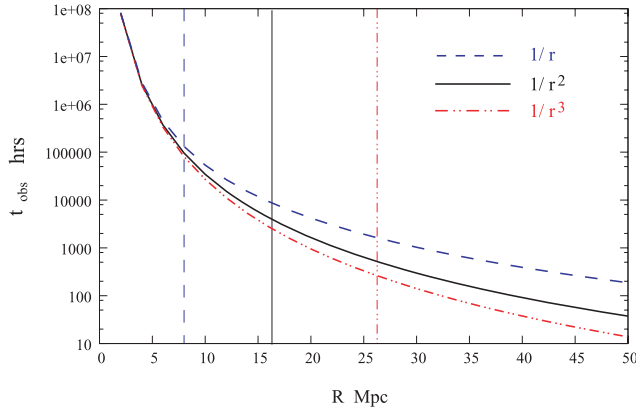

Figure 10. Same as Fig. 8 considering three different antenna distributions $\rho_{\rm ant}(r) \propto 1/r, 1/r^2, 1/r^3$ for the MWA.

required observing time increases rapidly with θ_c for off-centred bubbles.

When searching for bubbles in a particular observation, it will be necessary to consider filters corresponding to all possible value of R_b, ν_c and θ_c. A possible strategy would be to search at a discrete set of values in the range of R_b, ν_c and θ_c values where a detection is feasible. The crucial issue here would be the choice of the sampling density so that we do not miss out an ionized bubble whose parameters do not exactly coincide with any of the values in the discrete set and lie somewhere in between. To illustrate this we discuss the considerations for choosing an optimal value of $\Delta\theta_c$, the sampling interval for θ_c. We use $\langle\hat{E}\rangle[\Delta\theta]$ to denote the expectation value of the estimator when there is a mismatch $\Delta\theta$ between the centres of the bubble and the filter. The ratio Overlap $= \langle\hat{E}\rangle[\Delta\theta]/\langle\hat{E}\rangle[0]$, shown in Fig. 9 for GMRT (left-hand panel) and MWA (right-hand panel), quantifies the overlap between the signal and the filter as $\Delta\theta$ is varied. We see that the choice of $\Delta\theta$ would depend on the size of the bubble, we are trying to detect and it would be smaller for the GMRT as compared to the MWA. Permitting the Overlap to drop to 0.9 at the middle of the sampling interval, we find that it is 8 arcmin at the GMRT and 20 arcmin at the MWA for $R_b = 50\,{\rm Mpc}$.

The MWA is yet to be constructed, and it may be possible that an antennas distribution different from $\rho_{\rm ant}(r) \propto 1/r^2$, may improve the prospects of detecting H II bubbles. We have tried out $\rho_{\rm ant}(r) \propto 1/r$ and $1/r^3$ for which the results are shown in Fig. 10. We find that the required integration time falls considerably for the $1/r^3$ distribution whereas the opposite occurs for $1/r$. For example, for $R_b = 50\,{\rm Mpc}$ the integration time increases by 5 times for $1/r$ and

decreases by 3 times for $1/r^3$ as compared to $1/r^2$. Based on this we expect the integration time to come down if the antenna distribution is made steeper, but this occurs at the expense of increasing the HF and the foregrounds. We note that for the $1/r^3$ distribution, the foreground contribution is more than the signal, but it may be possible to overcome this by modifying the filter. The increase in the HF is inevitable, and it restricts the smallest bubble that can be detected to $R = 26\,{\rm MPc}$ for $1/r^3$. In summary, the $1/r^2$ distribution appears to be a good compromise between reducing the integration time and increasing the HF and foregrounds.

Finally, we examine some of the assumptions made in this work. First, the Fourier relation between the specific intensity and the visibilities equation (1) will be valid only near the centre of the field of view and full three-dimensional wide-field imaging is needed away from the centre. As the feasibility of detecting a bubble away from the centre falls rapidly, we do not expect the wide-field effects to be very important. Further, these effects are most significant at large baselines whereas most of the signal from ionized bubbles is in the small baselines.

Inhomogeneities in the IGM will affect the propagation of ionization fronts, and the ionized bubbles are not expected to be exactly spherical (Wyithe et al. 2005). This will cause a mismatch between the signal and the filter which in turn will degrade the S/N. In addition to this, in future, we plan to address a variety of other issues like considering different observing frequencies and making predictions for the other upcoming telescopes.

Terrestrial signals from television, FM radio, satellites, mobile communication etc., collectively referred to as RFI, fall in the same frequency band as the redshifted 21-cm signal from the reionization epoch. These are expected to be much stronger than the expected 21-cm signal, and it is necessary to quantify and characterize the RFI. Recently, Bowman et al. (2007) have characterized the RFI for the MWA site on the frequency range 80–300 MHz. They find an excellent RFI environment except for a few channels which are dominated by satellite communication signal. The impact of RFI on detecting ionized bubbles is an important issue which we plan to address in future.

The effect of polarization leakage is another issue we postpone for future work. This could cause polarization structures on the sky to appear as frequency-dependent ripples in the foregrounds intensity. This could be particularly severe for the MWA.

REFERENCES

Barkana R., Loeb A., 2001, Phys. Rep., 349, 125
Becker R. H. et al., 2001, AJ, 122, 2850
Bharadwaj S., Ali S. S., 2004, MNRAS, 352, 142
Bharadwaj S., Ali S. S., 2005, MNRAS, 356, 1519
Bharadwaj S., Pandey S. K., 2005, MNRAS, 358, 968
Bowman J. D., Morales M. F., Hewitt J. N., 2006, ApJ, 638, 20
Bowman J. D. et al., 2007, AJ, 133, 1505
Chengalur J. N., 2003, in Chengalur J. N., Gupta Y., Dwarkanath K. S., eds, Low Frequency Radio Astronomy. National Center for Radio Astronomy (TIFR), Pune, p. 191
Choudhury T. R., Ferrara A., 2006, in Fabbri R., ed., Cosmic Polarization, preprint (astro-ph/0603149)
Choudhury T. R., Ferrara A., 2007, MNRAS, 380, L6
Cooray A., Furlanetto S. R., 2004, ApJ, 606, L5
Datta K. K., Choudhury T. R., Bharadwaj S., 2006, MNRAS, 378, 119
DiMatteo T., Perna R., Abel T., Rees M. J., 2002, ApJ, 564, 576
Fan X., Narayanan V. K., Strauss M. A., White R. L., Becker R. H., Pentericci L., Rix H-.W., 2002, AJ, 123, 1247
Fan X., Carilli C. L., Keating B., 2007, ARA&A, 44, 415
Furlanetto S. R., Zaldarriaga M., Hernquist L., 2004, ApJ, 613, 1
Furlanetto S. R., McQuinn M., Hernquist L., 2006, MNRAS, 365, 115
Furlanetto S. R., Oh S. P., Briggs F. H., 2006, Phys. Rep., 433, 181
Morales M. F., Hewitt J., 2004, ApJ, 615, 7
Oh S. P., 1999, ApJ, 527, 16
Page L. et al., 2007, ApJS, 170, 335
Santos M. G., Cooray A., Knox L., 2005, ApJ, 625, 575
Shaver P. A., Windhorst R. A., Madau P., de Bruyn A. G., 1999, A&A, 345, 380
Spergel D. N. et al., 2007, ApJS, 170, 377
Swarup G., Ananthakrishnan S., Kapahi V. K., Rao A. P., Subramanya C. R., Kulkarni V. K., 1991, Curr. Sci., 60, 95
Thompson A. R., Moran J. M., Swenson G. W., 1986, Interferometry and Synthesis in Radio Astronomy. John Wiley & Sons, New York, p. 160
Wyithe J. S. B., Loeb A., 2004, ApJ, 610, 117
Wyithe J. S. B., Loeb A., Barnes D. G., 2005, ApJ, 634, 715
Zaldarriaga M., Furlanetto S. R., Hernquist L., 2004, ApJ, 608, 622

APPENDIX A: RELATION BETWEEN VISIBILITY–VISIBILITY CORRELATION AND MAPS

In this appendix, we give the calculations for expressing the two visibility correlation in terms of the MAPS. We can write the visibility $V(\boldsymbol{U}, \nu)$ as a two-dimensional Fourier transform of the brightness temperature $T(\boldsymbol{\theta}, \nu)$ (see equation 1)

$$V(\boldsymbol{U}, \nu) = \left(\frac{\partial B}{\partial T}\right)_{\nu} \int d^2\theta\, A(\boldsymbol{\theta}, \nu) T(\boldsymbol{\theta}, \nu) e^{2\pi i \boldsymbol{\theta} \cdot \boldsymbol{U}}, \quad (A1)$$

where $(\partial B/\partial T)_{\nu}$ is the conversion factor from temperature to specific intensity and $A(\boldsymbol{\theta}, \nu)$ is the beam pattern of the individual antenna. The visibility–visibility correlation is then given by

$$\langle V(\boldsymbol{U}_1, \nu_1) V(\boldsymbol{U}_2, \nu_2)\rangle = \left(\frac{\partial B}{\partial T}\right)_{\nu_1} \left(\frac{\partial B}{\partial T}\right)_{\nu_2}$$
$$\times \int d^2\theta \int d^2\theta'\, A(\boldsymbol{\theta}, \nu_1) A(\boldsymbol{\theta}', \nu_2)$$
$$\times \langle T(\boldsymbol{\theta}, \nu_1) T(\boldsymbol{\theta}', \nu_2)\rangle e^{2\pi i (\boldsymbol{\theta} \cdot \boldsymbol{U}_1 + \boldsymbol{\theta}' \cdot \boldsymbol{U}_2)}. \quad (A2)$$

The correlation function for the temperature fluctuations on the sky would simply be the two-dimensional Fourier transform of the MAPS $C_{2\pi U}(\nu_1, \nu_2)$

$$\langle T(\boldsymbol{\theta}, \nu_1) T(\boldsymbol{\theta}', \nu_2)\rangle = \int d^2 U\, C_{2\pi U}(\nu_1, \nu_2) e^{-2\pi i (\boldsymbol{\theta} - \boldsymbol{\theta}') \cdot \boldsymbol{U}}. \quad (A3)$$

Using the above equation in (A2), we obtain

$$\langle V(\boldsymbol{U}_1, \nu_1) V(\boldsymbol{U}_2, \nu_2)\rangle = \left(\frac{\partial B}{\partial T}\right)_{\nu_1} \left(\frac{\partial B}{\partial T}\right)_{\nu_2}$$
$$\times \int d^2 U\, C_{2\pi U}(\nu_1, \nu_2)$$
$$\times \tilde{A}(\boldsymbol{U}_1 - \boldsymbol{U}, \nu_1) \tilde{A}(\boldsymbol{U}_2 + \boldsymbol{U}, \nu_2), \quad (A4)$$

where $\tilde{A}(\boldsymbol{U}, \nu)$ is the Fourier transform of the beam pattern $A(\boldsymbol{\theta}, \nu)$. If the beam pattern is assumed to be Gaussian $A(\boldsymbol{\theta}, \nu) = e^{-\theta^2/\theta_0^2}$, the Fourier transform too is given by a Gaussian function

$$\tilde{A}(\boldsymbol{U}, \nu) = \pi \theta_0^2 e^{-\pi^2 U^2 \theta_0^2}. \quad (A5)$$

Hence, the visibility correlation becomes

$$\langle V(\boldsymbol{U}_1, \nu_1) V(\boldsymbol{U}_2, \nu_2)\rangle = \left(\frac{\partial B}{\partial T}\right)_{\nu_1} \left(\frac{\partial B}{\partial T}\right)_{\nu_2} \pi^2 \theta_1^2 \theta_2^2$$
$$\times \int d^2 U\, C_{2\pi U}(\nu_1, \nu_2)$$
$$\times e^{-\pi^2 [(\boldsymbol{U}_1 - \boldsymbol{U})^2 \theta_1^2 + (\boldsymbol{U}_2 + \boldsymbol{U})^2 \theta_2^2]}, \quad (A6)$$

where θ_1 and θ_2 are the values of θ_0 at ν_1 and ν_2, respectively. Now, since the two Gaussian functions in the above equation are peaked around different values of $\boldsymbol{U}$, the integrand will have a non-zero contribution only when $|\boldsymbol{U}_1 + \boldsymbol{U}_2| < (\pi \max [\theta_1, \theta_2])^{-1}$. In case the typical baselines are much larger than the quantity $(\pi \max [\theta_1, \theta_2])^{-1}$, the integral above can be well approximated as being non-zero only when $\boldsymbol{U}_1 = -\boldsymbol{U}_2$. Then,

$$\langle V(\boldsymbol{U}_1, \nu_1) V(\boldsymbol{U}_2, \nu_2)\rangle \approx \delta_{\boldsymbol{U}_1, -\boldsymbol{U}_2} \left(\frac{\partial B}{\partial T}\right)_{\nu_1} \left(\frac{\partial B}{\partial T}\right)_{\nu_2}$$
$$\times \pi^2 \theta_1^2 \theta_2^2 C_{2\pi U_1}(\nu_1, \nu_2)$$
$$\times \int d^2 U\, e^{-\pi^2 \left[(\boldsymbol{U}_1 - \boldsymbol{U})^2 \left(\theta_1^2 + \theta_2^2\right)\right]}$$
$$= \delta_{\boldsymbol{U}_1, -\boldsymbol{U}_2} \pi \left(\frac{\theta_1^2 \theta_2^2}{\theta_1^2 + \theta_2^2}\right) \left(\frac{\partial B}{\partial T}\right)_{\nu_1} \left(\frac{\partial B}{\partial T}\right)_{\nu_2}$$
$$\times C_{2\pi U_1}(\nu_1, \nu_2) \quad (A7)$$

which is what has been used in equation (9).

In the continuum limit, the Gaussian $\tilde{A}(\boldsymbol{U}, \nu)$ can be approximated by a delta function, that is, $\tilde{A}(\boldsymbol{U}, \nu) \approx \delta_D^{(2)}(\boldsymbol{U})$ (which corresponds to the limit $\theta_0 \to \infty$); the visibility–visibility correlation is then given as

$$\langle V(\boldsymbol{U}_1, \nu_1) V(\boldsymbol{U}_2, \nu_2)\rangle = \delta_D^{(2)}(\boldsymbol{U}_1 + \boldsymbol{U}_2) \left(\frac{\partial B}{\partial T}\right)_{\nu_1} \left(\frac{\partial B}{\partial T}\right)_{\nu_2}$$
$$\times C_{2\pi U_1}(\nu_1, \nu_2), \quad (A8)$$

which corresponds to equation (21) in the main text.

This paper has been typeset from a TeX/LaTeX file prepared by the author.